Advantages and disadvantages of data analysis using semileptonic decay of the B^0 meson

W.A. Poorthuis
5726034

June 12, 2019

Supervisor:
Dr. A. Grelli
Institute for Subatomic Physics
Utrecht Univerity

Daily supervisor:
Dr. C. Bedda
Institute for Subatomic Physics
Utrecht Univerity

Daily supervisor
Dr. H.J. Correia Zanoli
Institute for Subatomic Physics
Utrecht Univerity

Abstract

In this thesis we studied the advantages and disadvantages of using a semileptonic decay channel to separate the signal of B^0 mesons from the background in high energy proton-proton collisions at the ALICE experiment. The advantages offered by this approach are that there are extra variables in which one can apply cuts to separate signal from background. Disadvantages of this approach a lower branching ratio than certain hadronic decay channels and most significantly missing neutrino energy. This missing energy can be reconstructed, albeit only in approximation.

Contents

1 Introduction

Almost 14 billion years ago, the universe sprang into existence with the big bang. It was extremely dense and hot, but expanded rapidly. After 10^{-12} seconds, temperature and density were such that a quark-gluon plasma (QGP) could form [1]. In this form of matter, quarks and gluons travel freely, without being bound to one another. At the beginning of the universe they travelled with relativistic speeds. As the universe expanded further, the temperature and pressure dropped, the QGP dissolved and finally the elementary particles began to coalesce into ordinary matter, into stars, galaxies and planets.

The ALICE Detector at CERN is designed to study QGP in a controlled environment. By colliding lead nuclei at relativistic speeds, for a brief moment the energy and density inside the detector are both so high that a QGP is able to form. From this plasma, particles emerge that can be detected. The characteristics of these particles can tell us something about the QGP inside the detector, helping us understand its properties. We can then use our understanding of the QGP to help us understand the beginning of the universe itself.

One of the particles used to infer the characteristics of the QGP is the B^0 meson. However, to measure the effect of the QGP on B^0 mesons, we first need to be able to single out the decay daughters of the B^0 from the background of other particles we detect.

In this thesis we will look at a possible way to improve the reconstruction of the B^0 meson. We will do this by using one of its semileptonic decay channels, instead of a hadronic decay channel. In this thesis we simulate B^0 mesons in pp collisions. This collision system is used as a reference for studies heavy-ion collisions. This is useful as a benchmark to disentangle the effects of the QGP from other effects.

We will first take a look at the theory underlying these decays, the standard model and the QGP in chapter 2. Then we will explore how the ALICE detector collects data in chapter 3. In chapter 4 we will explain the methods used to perform the research. The results will be displayed in chapter 5 and we will end with a discussion and conclusion in chapter 6.

2 Theoretical background

2.1 Standard Model

The standard model is the theory most successful in describing all fundamental particles and their interactions, although there exist many phenomena unexplained by the standard model. Nagashima [2] summarizes the essence of the standard model using the following three phrases:

1. "Building blocks of matter are quarks and leptons"
2. "Their interactions are described in the mathematical framework of the gauge field theory."
3. "The vacuum is in a sort of superconducting phase."

The first phrase denotes that quarks and leptons are fundamental particles. They cannot be split into smaller constituents and all matter consists of them. An overview of the fundamental particles, including force carriers, is given in Figure 1.

The second phrase tells us that how these fundamental particles, and thus all matter, interacts is described by gauge field theory. The gauge theories that are incorporated into the standard model are: electromagnetism, the weak force, which are at high energy scales unified in the electroweak force, and the strong force. These forces are with the addition of gravity, the fundamental forces. The integration of gravity into the standard model is an area of active research in theoretical physics. The history and prospects of unifying forces can be seen in Figure 2.

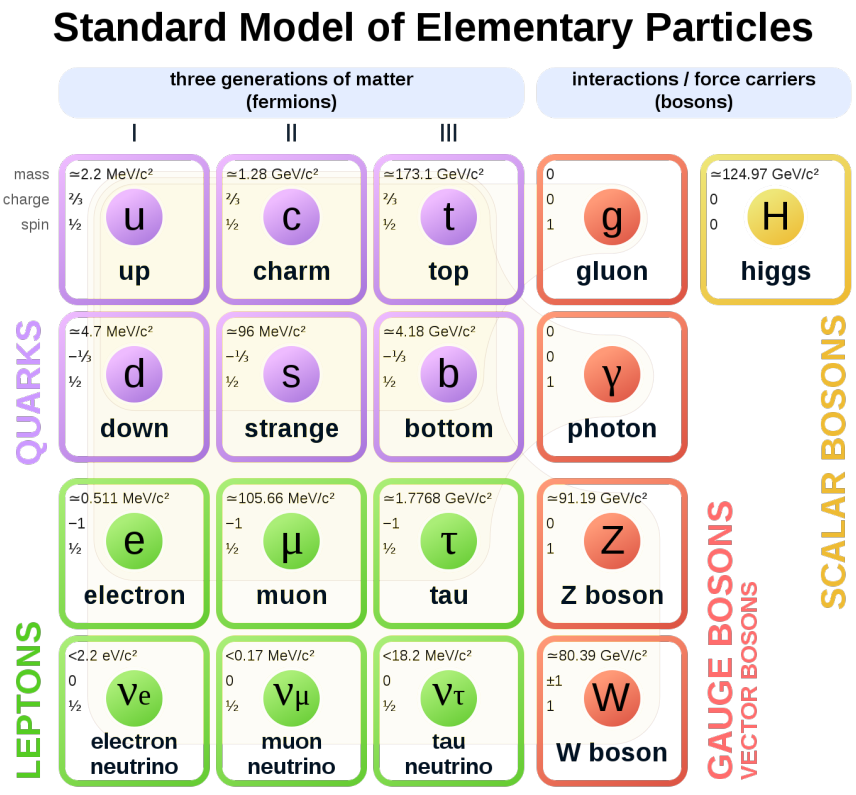

Figure 1: Overview of the elementary particles and force carriers in the standard model. [3]

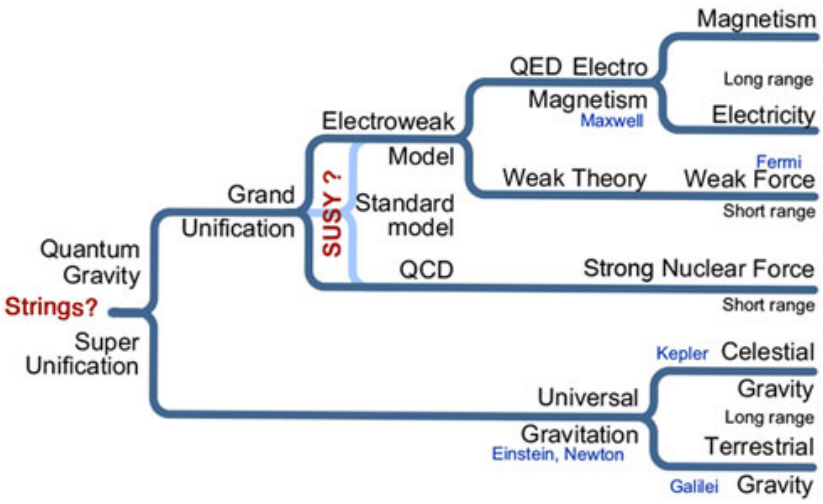

Figure 2: Overview of the past and possible future unification of forces. [4]

FORCE	Mediating Particle	Range	Strength
Gravity	Graviton	Long $(1/r^2)$	10^{-38}
Weak	W^+, W^-, Z bosons	Short (≈ 0.001 fm)	10^{-9}
Electromagnetism	Photon	Long $(1/r^2)$	1/137
Strong	Gluon	Short (≈ 1 fm)	1

Figure 3: Overview of the forces, their force carriers, range and coupling constant. [5]

These fundamental forces all interact with matter in a different way; they couple to different properties of particles. Gravity couples to mass, electromagnetism to electric charge, the weak force to weak isospin, and the strong force couples to colour charge. This coupling happens through force carrier particles. These particles are manifestations of the fields required by quantum mechanics and the ones in the standard model are also incorporated in Figure 1.

The final phrase refers to the Higgs mechanism. This is the mechanism through which particles attain their mass. A detailed explanation is beyond the scope of this thesis, as it is not necessary to understand the experiment.

The fundamental forces can be split into two groups as can be seen in Figure 3. There are long ranged and short ranged forces. Because we will be dealing with subatomic distances, we will take a closer look at strong force, because it is short ranged and dominates that domain.

2.2 Strong force

The strong force is the force that holds quarks together in hadrons. The theory that describes this interaction quantum chromodynamics (QCD) is characterized in two principles: confinement and asymptotic freedom.

In their normal state, quarks and gluons are never found alone. This is called colour confinement. They are always found together in so called hadrons, of which there are two types: mesons, which consist of a quark and an antiquark, and baryons, which consist of three quarks or antiquarks. The gluons are the force carriers of the strong force and they hold the hadrons together.

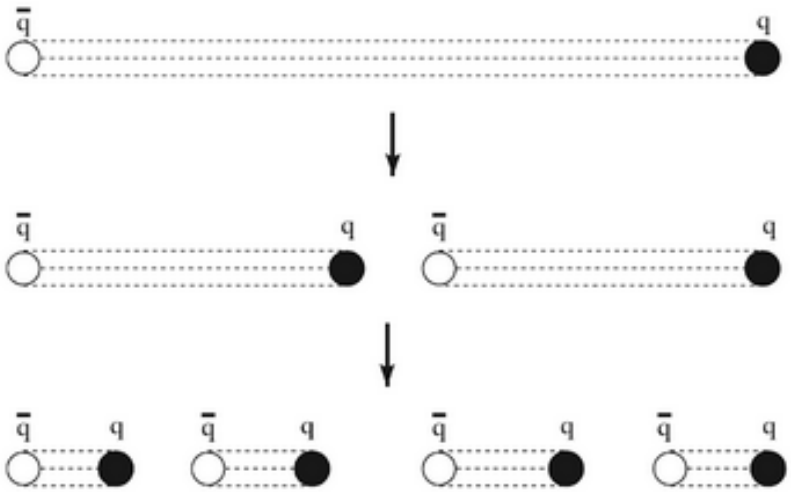

Figure 4: Creation of quark-antiquark pair by separation of quarks. [7]

There is no analytical proof as to why this happens, but it can be qualitatively understood. Confinement is thought to happen because, in order to separate two quarks, further increasing amounts of energy are needed because of self-interacting gluons. Following [6], to approximation, this potential is given by

$$V_{q\bar{q}}(\vec{r}) = -\frac{4\alpha_S(Q^2)}{3r} + \kappa r. \tag{1}$$

Here, α_S is the coupling constant, r is the absolute distance between two quarks and κ is the string tension constant. The coupling constant is a measure of the strength of a force and the string tension constant tells us how much energy is needed to further separate the quarks. When two quarks are separated it eventually becomes energetically favourable to create a quark-antiquark pair and the separated quarks are still bound into hadrons as can be seen in Figure 4.

Asymptotic freedom refers to the fact that as interacting quarks exchange more momentum, the coupling constant of the strong force gets smaller. Again, as per [6], the coupling constant is, to first-order approximation, defined as:

$$\alpha_S(Q^2) = \frac{12\pi}{(11N_c - 2N_f)\cdot \ln(Q^2/\Lambda^2_{QCD})}, \tag{2}$$

with Q the momentum transfer, $N_c = 3$ the number of different colour charges, N_f the number of quark flavours with a mass below the used normalisation scale and $\Lambda_{QCD} \approx 200$ MeV a scale parameter that also depends upon the normalisation scale. We see that as the momentum transfer grows, the coupling constant decreases.

2.3 Quark gluon plasma

In contrast to the above, in a QGP quarks and gluons are not confined in hadronic states and they move as if they were free particles. This happens because at increasing density, the amount of quarks per hadronic volume is higher than meaningful for a partitioning into colour-neutral hadrons. This increase in density can be achieved by compressing the matter or the matter being at a high enough temperature. [8] The threshold for a QGP to form is ~ 200 MeV ($\sim 2 \cdot 10^{12}$ K) [1].

QGP can be created in the laboratory by colliding heavy ions, in the case of the ALICE experiment lead ions are used. in these Pb-Pb collisions the properties of the QGP can be studied. There are however

other collision systems, which are used to disentangle the effect of the QGP from other sources. In p-p collisions no QGP is formed and QCD is applicable. This helps us understand the production properties of the collisions. P-Pb collisions help further our understanding of cold nuclear matter effects. Thus the data from these collisions can be used to help identify the non-QGP effects in a collision, which in turn allows us to disentangle non-QGP and QGP effects.

2.4 B^0 meson

The B^0 meson consists of a bottom antiquark and a down quark. Its rest mass is 5279.64 ± 0.13 MeV/c^2 [9]. We are interested in the B^0 meson because one of its quarks, the bottom antiquark, has a high mass, namely $4.18^{+0.04}_{-0.03}$GeV/c^2 [9]. An important consequence of this fact is that the quark, when it is inside the QGP, will not reach thermal equilibrium, but it *will* get affected by the QGP. This means that, when it leaves the QGP and gets into a bound state as a B^0 meson, we can study the effects of the QGP on that quark by comparing the characteristics of the B^0 to the characteristics of a B^0 which consists of quarks that were not affected by the QGP. [10]

Furthermore, the B^0 is an unstable particle that can decay via a large amount of decay channels. The high mass of the B^0 means that it decays quickly, but its characteristics influence those of the decay daughters, which we can detect. Some decay channels are hadronic, meaning all daughter particles in the decay chain are hadrons, and some are semileptonic, meaning that there are hadrons *and* leptons present in the decay chain. These decay channels are not all accessed equally often and the associated branching ratio (BR) tells us how often a B^0 meson decays according to that channel. The branching ratio of a decay mode i is defined as:

$$BR_i = \frac{\Gamma_i}{\Gamma_{total}}. \tag{3}$$

Γ is the decay width of a certain decay which is related to its lifetime by $\tau = \frac{1}{\Gamma}$, where τ is the time needed for an ensemble of particles to shrink to $\frac{1}{e}$ its original size.

The decay channel that we are interested in is:

$B^0 \to D^- e^+ \nu_e$	BR = $(2.31 \pm 0.10) \cdot 10^{-2}$	[9]
$D^- \to K^+ \pi^- \pi^-$	BR = $(9.38 \pm 0.16) \cdot 10^{-2}$	[9]
For a total of		
$B^0 \to e^+ \nu_e K^+ \pi^- \pi^-$	BR = $(2.2 \pm 0.1) \cdot 10^{-3}$	

This is a semileptonic decay channel. We will use this channel because it has a relatively large branching ratio, so it will provide more data than other semileptonic decay channels. However, there is a caveat. As we will see in the following chapter, the electron neutrino ν_e cannot be detected, so its properties will have to be reconstructed.

Another decay channel that be are interested in is a particular hadronic decay channel:

$B^0 \to D^- \pi^+$	BR = $(2.52 \pm 0.12) \cdot 10^{-3}$	[9]
$D^- \to K^+ \pi^- \pi^-$	BR = $(9.38 \pm 0.16) \cdot 10^{-2}$	[9]
For a total of		
$B^0 \to K^+ \pi^- \pi^- \pi^+$	BR = $(2.36 \pm 0.12) \cdot 10^{-4}$	

The daughters in this decay chain are similar to the ones from the semileptonic decay. This means that we can easily compare their characteristics. It is also a realistic decay channel to look at because it has a a relatively high BR for a hadronic decay [6]. We will use this hadronic decay channel to compare the results of a simulation using the semileptonic decay to those of a more conventional decay channel.

3 Experimental background

The ALICE Detector is hosted at CERN and its main goal is to research QGP. It does so by creating a QGP in the LHC, the Large Hadron Collider. This is the biggest particle accelerator in the world. Here packets lead nuclei are collided at center-of-mass energies of 5.02 TeV per nucleon pair. Particles produced in these collisions are measured in the ALICE detector and then processed.

The ALICE detector consists of 19 subdetectors, as can be seen in Figure 5. [11] These detectors are all capable of measuring certain properties of the particles that pass through them and by combining this information, we can reconstruct the characteristics of those particles. The, for our purposes, most relevant detectors are described in the following paragraphs.

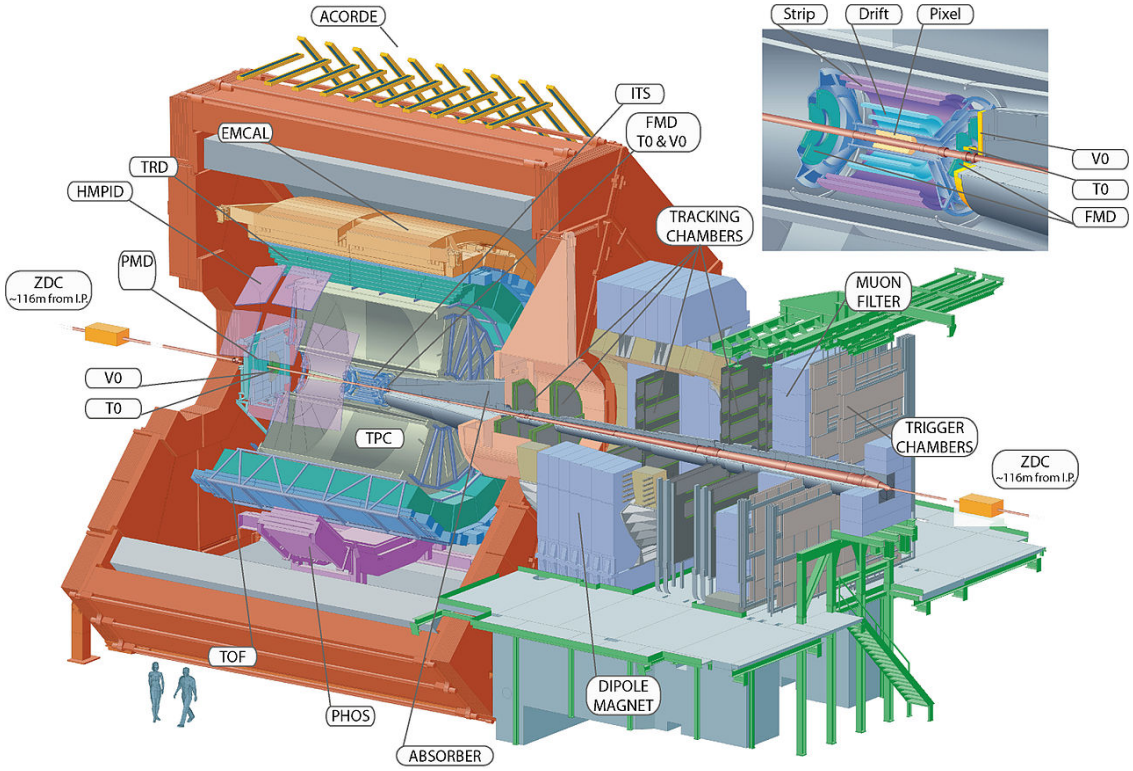

Figure 5: Computer generated cut-away view of ALICE detector, showing the 19 detectors inside. [12]

The detector closest to the point of impact is the Inner Tracking System (ITS). This detector is built out of six layers of silicon detectors. These detectors provide information about the path a particle takes. The main function of the ITS is to reconstruct primary and secondary vertices. [13] The primary vertex is the collision point, while the secondary vertex is the point where a particle decays. This point can be reconstructed by looking at the paths the daughter particles take ans extrapolating from there.

The next detector a particle encounters on its journey away from the primary vertex is the Time Projection Chamber (TPC). It is a chamber filled with a gas, of which the atoms get ionized as charged particle pass through the gas. The electrons that get liberated in this way drift towards end plates where the signal gets transmitted. The detector can identify the paths taken by particles and measure their momentum. [14]

The Time of Flight (ToF) detector is located outward from the previous two. This detector is used to measure the velocity of the particle, by measuring the time it takes a particle to cross a certain distance along the track trajectory. When both the velocity and the momentum are known, the mass of a particle can be calculated. [15]

The, for our studies, relevant characteristics that can be reconstructed from the data provided by the

detectors are: transverse momentum (p_T), pseudorapidity (η), invariant mass (m_0), the decay length and the pointing angle.

The transverse momentum denotes the momentum of the particle perpendicular to the beam axis. This axis is generally taken to be the z-axis and then $p_T = \sqrt{p_x^2 + p_y^2}$.

Pseudorapidity is defined as $\eta = -\ln \tan \frac{\theta}{2}$, wherein θ is the angle between the particle momentum and the positive direction of the beam axis. This relationship between θ and η is graphically shown in Figure 6

The invariant mass m_0 is the mass of a particle. It can be calculated in any frame by $m_0^2 c^2 = (\frac{E}{c})^2 - \|p\|^2$, with E the energy of the particle, c the speed of light and $\|p\|$ the norm of the particles momentum. In a particle decay, energy and momentum are conserved. This allows us to reconstruct the invariant mass of the B^0 meson.

The decay length is the distance travelled by an unstable particle before it decays. This can be from the collision vertex to a decay vertex, or from a particular decay where a particle is created vertex to the decay vertex of that particle.

The pointing angle is the angle between the vector between the primary and secondary vertex and the momentum of the reconstructed mother particle. The momentum of this particle can be reconstructed by matching its daughter particles, which we can detect, and inferring it from their properties.

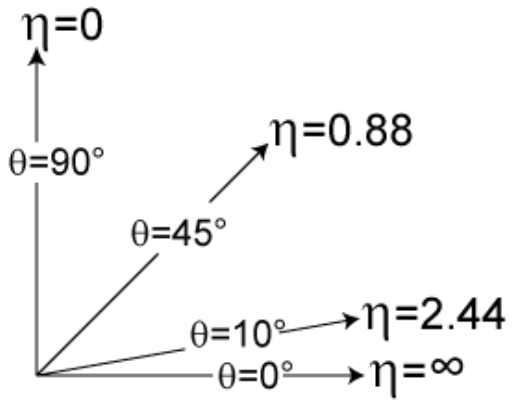

Figure 6: As θ approaches 0, η goes to infinity. [16]

However, not everything is measurable. The electron neutrino that is produced in the decay of the B^0 is almost impossible to measure, because neutrinos interact very weakly with other matter, so it will pass through all the detectors without interacting. This means that we will not have all the information available to us whilst reconstructing the characteristics of the B^0. In order to be able to gather information about the B^0, we will need to reconstruct the properties of the ν_e from the information we *do* have, as will be further explained in chapter 4.2.

4 Methodology

In this chapter, the methodology of the simulations and the data analysis will be discussed. Both simulations are Monte Carlo simulations, although they are done in different programs and have different characteristics.

4.1 Pythia simulations and analysis

The first set of simulations was done in PYTHIA 8.240 [17]. This is a program built for simulating high energy collisions, similar to those done in a particle accelerator like the LHC. This PYTHIA framework was then integrated into ROOT 6.16/00, which is a program that provides the functionalities needed to analyse and visualize the data generated by PYTHIA [18]. These simulations do *not* take the capabilities of the detector into account, but they are still useful, because from these simulations we can learn about the decay kinematics and its properties, even if we don't have all the information which will be available in data. In this thesis, these simulations have been used to study the effects of cuts in the p_T of the B^0 on the the characteristics of the B^0 and the daughter particles.

PYTHIA has a variety of modes to simulate a variety of different processes. For our purposes, the mode *HardQCD* was appropriate. In this mode we enabled the B meson heavy flavour flag *hardbbar*. This enables PYTHIA to simulate $gg \to b\bar{b}$ and $q\bar{q} \to b\bar{b}$ processes. Furthermore, the simulation was done three times, each time with different decays enabled. This was done to isolate the effects of a particular decay chain. In each run, one million events were simulated for proton-proton collisions at a center-of-mass energy of 7 TeV.

The semileptonic run was done with, for B^0 and D^- mesons, only the decays $B^0 \to D^- e^+ \nu_e$, $D^- \to K^+\pi^-\pi^-$ enabled. This is the decay chain that we are interested in.

The hadronic run was done with, for B^0 and D^- mesons, only the decays $B^0 \to D^-\pi^+$, $D^- \to K^+\pi^-\pi^-$ enabled. This is the hadronic decay mentioned in Chapter 2.4.

The third run was done with all decays enabled. This run simulates the background that would be found in the experiment. However, charm and beauty quark production is still forced. Instead of only accepting particles that have a B^0 as a mother in their decay chain, all B^0, D^-, e^+, ν_e, K^+ and π^- were taken into account. This also means that there were no p_T cuts done.

The data stored from these simulations are the p_T and η of each particle in the decay chain. For the daughter particles, the difference between its own η and its mothers η was also calculated.

4.2 ALICE simulation and analysis

The other simulation is a Monte Carlo simulation wherein the response of the whole ALICE detector is also simulated. 28 million events were generated and in each event, one charm of beauty quark is generated from proton-proton collisions at 7 TeV. Due to some applied pre-selection, the data for the p_T range between 0 GeV/c and 3 GeV/c was not saved. In the simulation, a variety of variables was stored. These variables are used to cut away certain data that does not fit these criteria and to reconstruct the invariant mass of the B^0 candidates. To get these B^0 candidates several steps were undertaken.

Firstly, D^- candidates were reconstructed from three tracks that are possibly two π^- and one K^+. Secondly, all tracks in the same event were looped over to associate a possible e^+ to the D^- candidate. Thirdly, these two were taken together to be a B^0 candidate, or $D^- e^+$ object. Note that the ν_e is not taken into account, because the ALICE detector generally doesn't detect those particles. This means the B^0 candidate has a lower invariant mass than it should, because the energy from the ν_e is missing.

This reconstruction was done for all particles, which means most of the B^0 candidates are not B^0 mesons at all. However, some of those candidates are B^0 and it is possible to match the B^0 candidates to the neutrino energies, to create these true B^0 mesons, which we will call the matched B^0 candidates. These are used in the analysis to compare the signal we get from the $D^- e^+$ objects after we cut in certain variables, telling us how effective our cuts are.

The cuts made to the data for the analysis are listed in Table 1. They were established by taking into account the significance, defined as

$$significance = \frac{signal}{\sqrt{signal + background}}, \tag{4}$$

of the signal. By making two dimensional histograms, of which an example can be seen in Figure 7, this significance can be made visual. In these histograms, the significance increases cumulative from the We aimed for a significance higher than 3 for our cuts, while keeping in mind the amount of signal and background particles.

Cuts per B^0 p_T bin	[GeV/c]		$3 < p_T < \text{inf}$	$3 < p_T < 6$	$6 < p_T < 10$	$10 < p_T < \text{inf}$
B^0 pointing angle	$[\cos\theta]$	$>$	0.98	0.98	0.98	0.98
B^0 decay length	[cm]	$>$	6	3	6	6
D^- pointing angle	$[\cos\theta]$	$>$	0.98	0.98	0.98	0.98
D^- decay length	[cm]	$>$	12	8	12	12
D^- mass (within 2σ)	[GeV/c^2]	$=$	1.869	1.869	1.869	1.869

Table 1: Cuts made to the D^-e^+ objects per B^0 p_T bin [GeV/c^2].

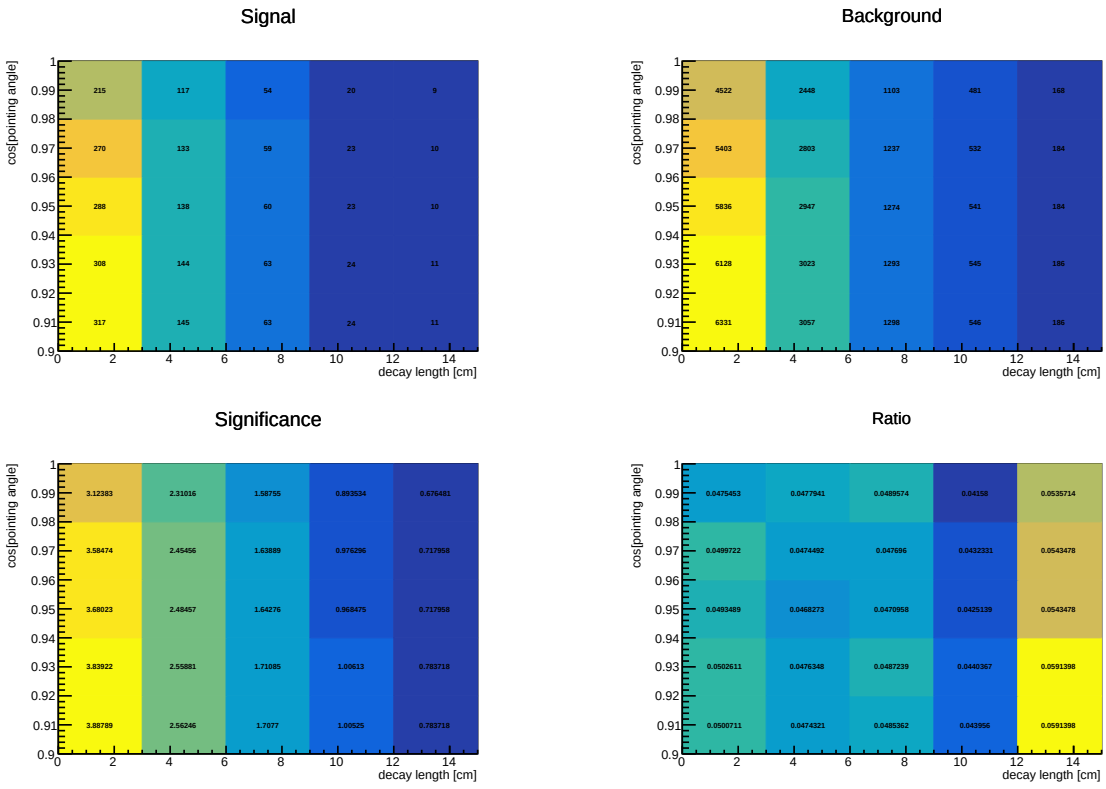

Figure 7: Two dimensional histograms with the signal, background, and their significance and ratio ($\frac{signal}{bcakground}$) for 3 GeV/c $< p_T^{B^0} <$ inf GeV/c in the parameters B^0 decay length and B^0 pointing angle.

Because the neutrino energy is missing, we need to reconstruct it to get a better value for the mass of the B^0. This is done by reconstructing the missing energy as the component of the B^0 momentum perpendicular to its flight path ($p_{T_{missing}}$). The geometric justification for this method can be seen in Figure 8. Using this $p_{T_{missing}}$ we correct the invariant mass by using the equation

$$m_{0_{corrected}} = \sqrt{m_0^2 + \left|p_{T_{missing}}\right|^2} + \left|p_{T_{missing}}\right|. \tag{5}$$

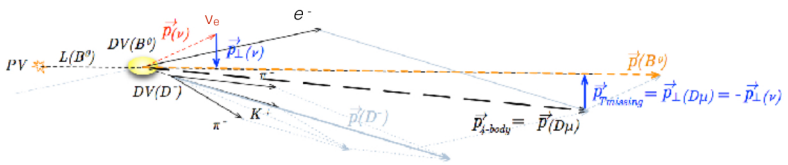

Figure 8: The geometry of the reconstruction of the $p_{T_{missing}}$.[19]

5 Results

In this chapter, the result from the two simulations are shown. The first three sub-chapters will be be on the results of the PYTHIA simulation and the fourth will be on the the ALICE simulation.

5.1 p_T distributions

In this section we will discuss the p_T distributions generated in the PYTHIA simulation. In Figure 9 we see that in total, the D^- coming from the semileptonic decay have a lower p_T than those coming from the hadronic decay, although both are higher than the background, represented by the unforced decay. We also see that as the p_T of the mother B^0 gets higher, both distributions get wider. With a p_T of the B^0 between 3 and 18, the distribution of the hadronic decay channel is not peaked, but it has a flattened top. As the p_T of the B^0 gets higher, the distributions become much less clear. We also see that, at a p_T of the B^0 mother lower than 3 GeV/c^2 the distribution for the p_T of the D^- of semileptonic decay seems to be almost the same as the background, with the hadronic decay being slightly wider. This means that the hadronic decay is a slightly better suited for analysis, since more background can be cut. However, as the p_T of the mother increases, the semileptonic and hadronic distributions shift to higher p_T and get progressively wider. This means that in the higher p_T ranges, a lot of background can be cut away using both the semileptonic and hadronic decays. Taken over the entire p_T range, the distribution is slightly wider than the background, but peaks at almost the same p_T, with the hadronic decay being a bit wider still.

In the distributions of the p_T of the K^+, shown in Figure 10, the p_T distribution of hadronic decay is also wider than the distribution of the semileptonic decay, although the difference between the two channels is much smaller. For a p_T of the B^0 lower than 3 GeV/c^2, all three distributions are similar, meaning that it is hard to make a p_T cut to remove background. At higher p_T cuts, the distribution gets wider. However, in contrast to the distribution of the p_T of the D^-, the distributions for the K^+ retain their lower p_T part. Here, there doesn't seem to be any flattening of the peak of the hadronic distribution. There is however the fact that at higher p_T of the B^0, the distribution becomes less clear, although the effect is smaller than for the D^-. The background is also more sharply peaked at low p_T than the background of D^- mesons. The fact that the background is so sharply peaked means that it is easier to cut it away.

As shown in Figure 11, in the case of the π^- there is a noticeable difference too between the three distributions, although at higher p_T of the B^0, the difference between the semileptonic and hadronic distributions gets increasingly smaller. In the first three p_T bins, the distributions hardly change, however in the last two bins the distributions widen, although here, the peak of the distribution for the semileptonic and hadronic decays stay at low p_T, instead of moving to higher p_T. This means that when a p_T cut to remove the background is made, relatively much of the signal will also be lost. The π^- background also has a sharp peak at low p_T, like the background of the K^+.

In contrast to the previously observed daughters, which were all meson, we can see in Figure 12 and Figure 13 two leptonic daughters. Thus, there is no distributions for the hadronic decay channel. The two p_T distributions that are shown differ from the pattern we previously saw. The background is still very sharply peaked, as can be seen by their low mean values, but the p_T distributions of the daughters are much less so. The distributions still get wider at higher p_T cuts, but their maximum moves to lower p_T and their slopes get flatter. In the case of the e^+, the bulk of the distribution lies outside of the background distribution. This helpful when trying to make a p_T cut to remove background, because a lot of the signal will survive the cut.

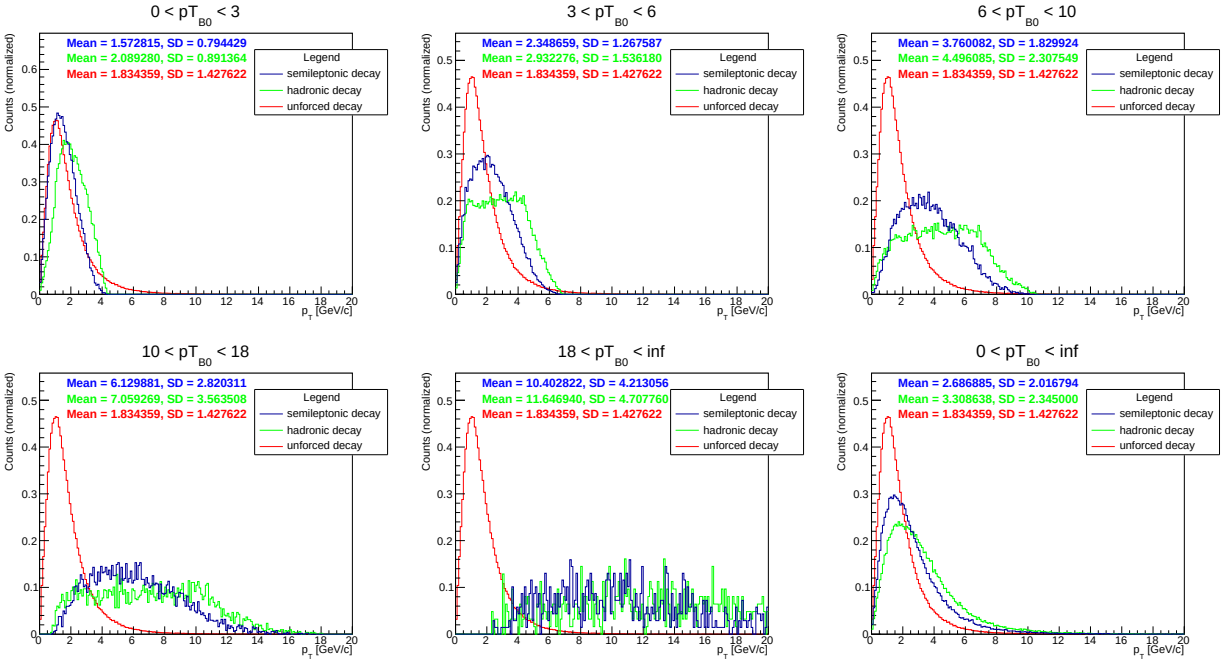

Figure 9: Comparison of p_T distributions for D^- mesons in semileptonic, hadronic and unforced decays.

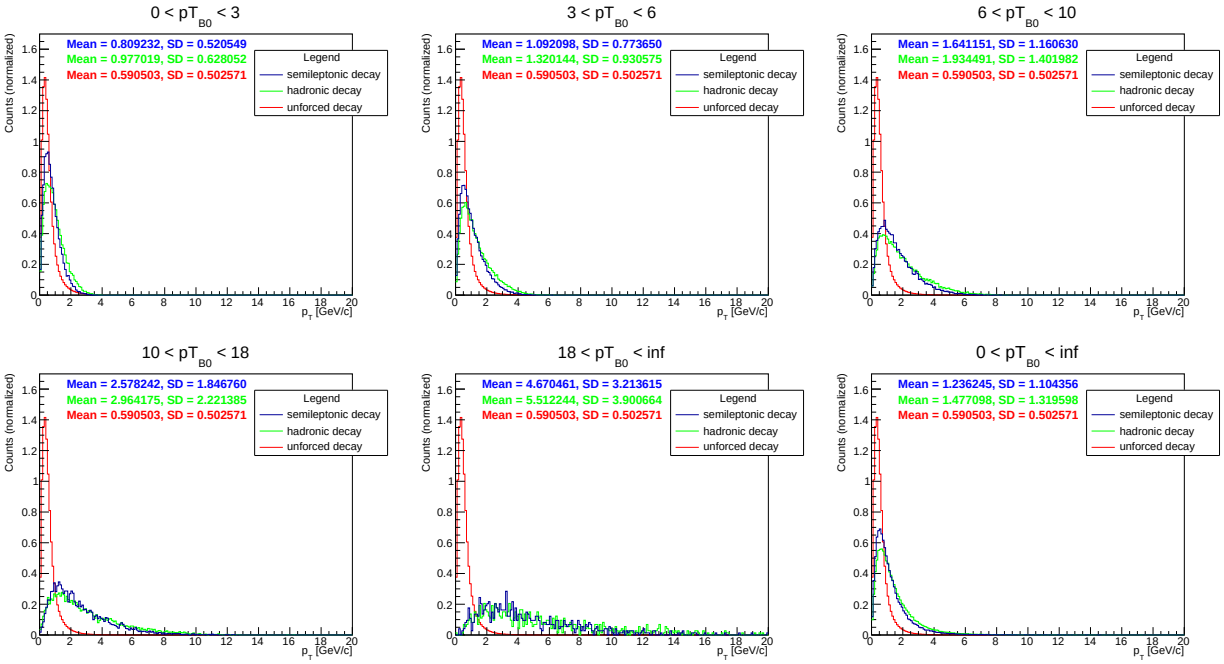

Figure 10: Comparison of p_T distributions for K^+ mesons in semileptonic, hadronic and unforced decays.

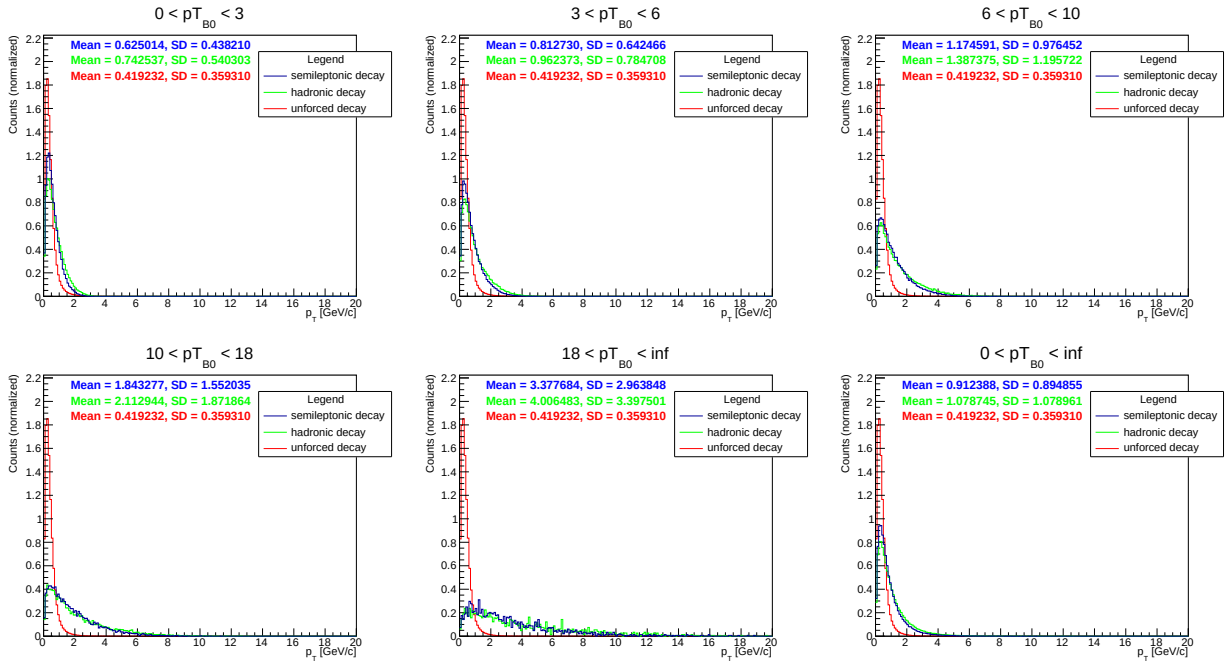

Figure 11: Comparison of p_T distributions for π^- mesons in semileptonic, hadronic and unforced decays.

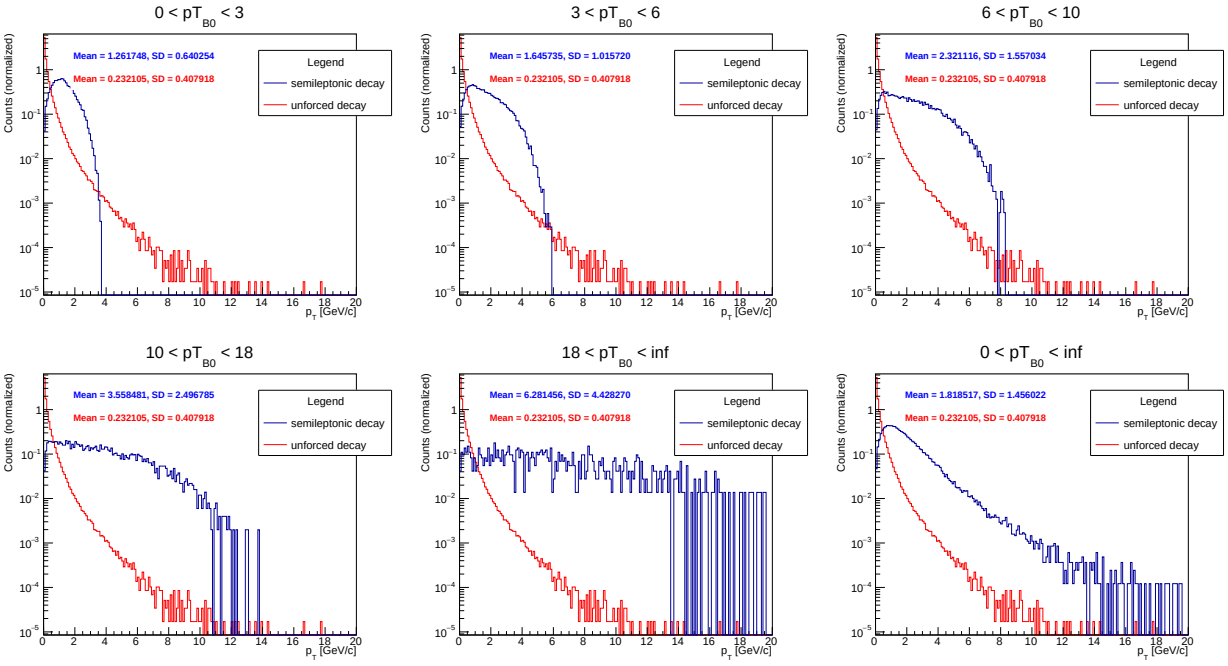

Figure 12: Comparison of p_T distributions for e^+ in semileptonic and unforced decays.

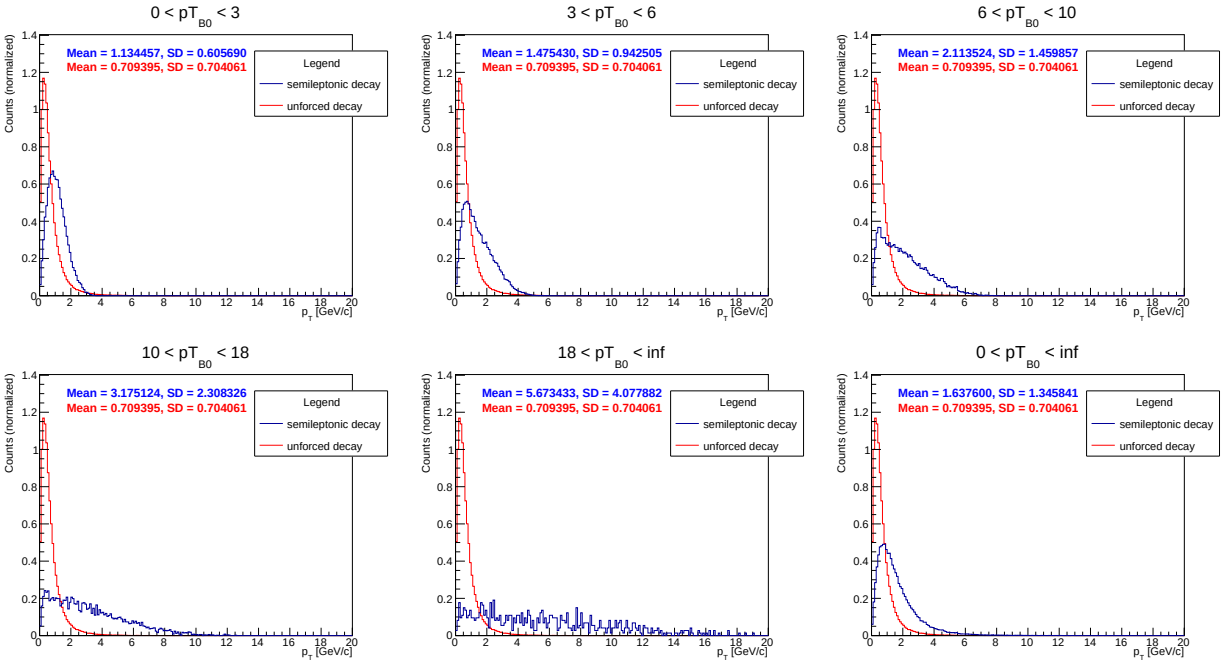

Figure 13: Comparison of p_T distributions for ν_e in semileptonic and unforced decays.

5.2 η distributions

In this section we will discuss the η distributions generated in the PYTHIA simulation. In Figure 14 the pseudorapidity distributions of the D^- can be seen. The distributions of the semileptonic and the hadronic decay channel agree with each other to great extent. All three distributions have two peaks, although with the distributions of the two decay channels, these gradually disappear as we get to the higher regions. This means the relative difference between the background and the signal increases, which can be taken advantage of by imposing a cut on the maximum η. Integrated over the entire p_T range, the peaks are still present. When we compare these distributions with the background, we seen that overall, D^- coming from the semileptonic and hadronic decay channel have a η closer to zero, signified by the narrower distributions. Furthermore, the distributions get narrower as we move into higher p_T bins. This means that imposing a looser cut on the maximum η can cut away background while retaining the signal.

Figure 15 shows a similar pattern. Here, the two decay channel distributions are alike too. However, for them, the two peaks are less pronounced than in the case of the D^-. The background distribution however, still has the pronounced peaks. This means a cut on the maximum η of the K^+ will be more effective at lower $p_T^{B^0}$ compared with one for the D^-. Nevertheless, taken over the entirety of the p_T range, we do still see a small dip in the peaks of the semileptonic and hadronic decay distributions. The narrowing of the distributions is also still present.

In the case of the π^-, the two peaks are much less pronounced in the background and absent in the two other distributions, as can be seen in Figure 16. A cut on the maximum η will thus be less effective, because the relative difference between background and signal is smaller. The hadronic and semileptonic decays are still in agreement with each other and their distributions still get narrower as the p_T of the B^0 gets higher.

In Figure 17, we see the distributions of the semileptonic decay and the background of the e^+. The hadronic decay is absent, because there are no e^+ in its decay chain. The distribution of the semileptonic decay chain is narrower than the background in each p_T bin and gets narrower as the p_T of the B^0 mother increases. There is no sign of the two peak structure we saw earlier. Therefore, only a loose cut on the maximum η will be effective.

In Figure 18 the distributions of the ν_e are shown. These look similar to the ones of the e^+, there is just one peak, but the background and decay distributions are more similar in width. However, the distribution of the semileptonic decay does get narrower as the p_T of the B^0 mother increases.

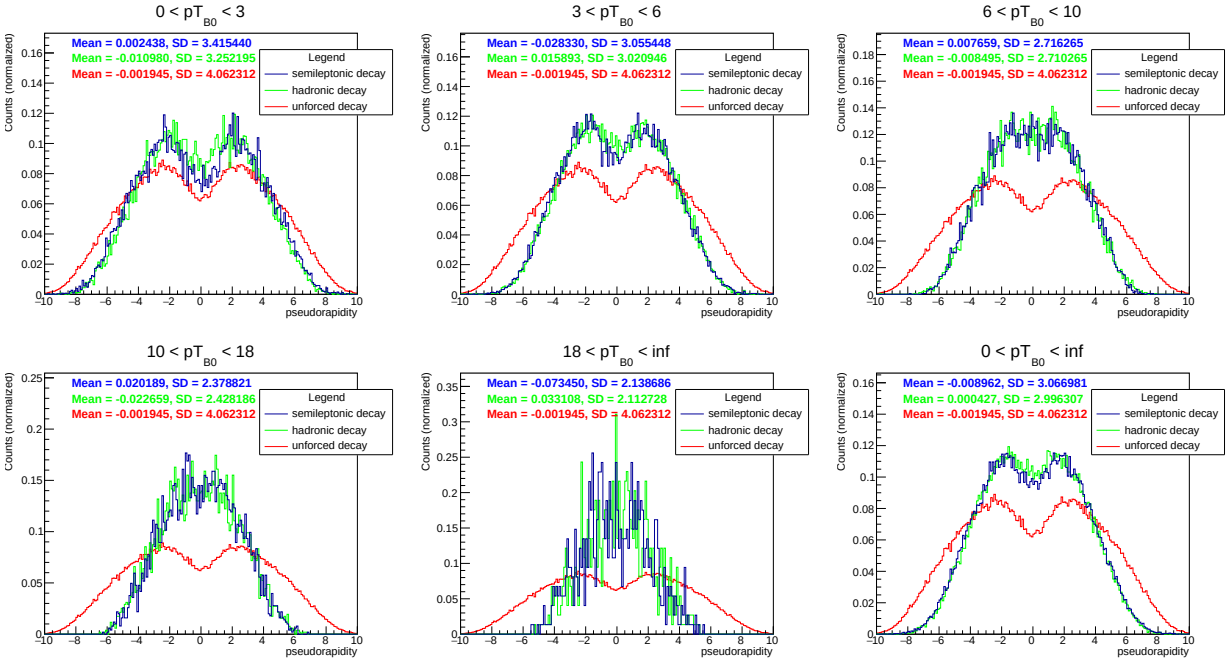

Figure 14: Comparison of η distributions for D^- in semileptonic, hadronic and unforced decays.

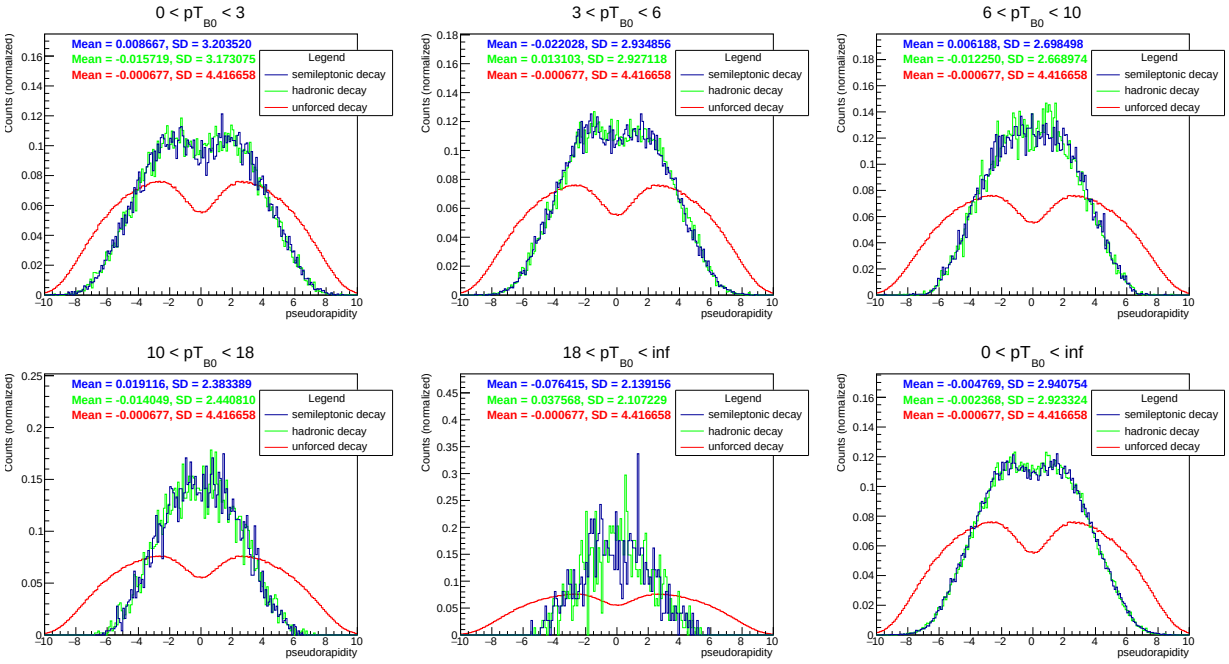

Figure 15: Comparison of η distributions for K^+ in semileptonic, hadronic and unforced decays.

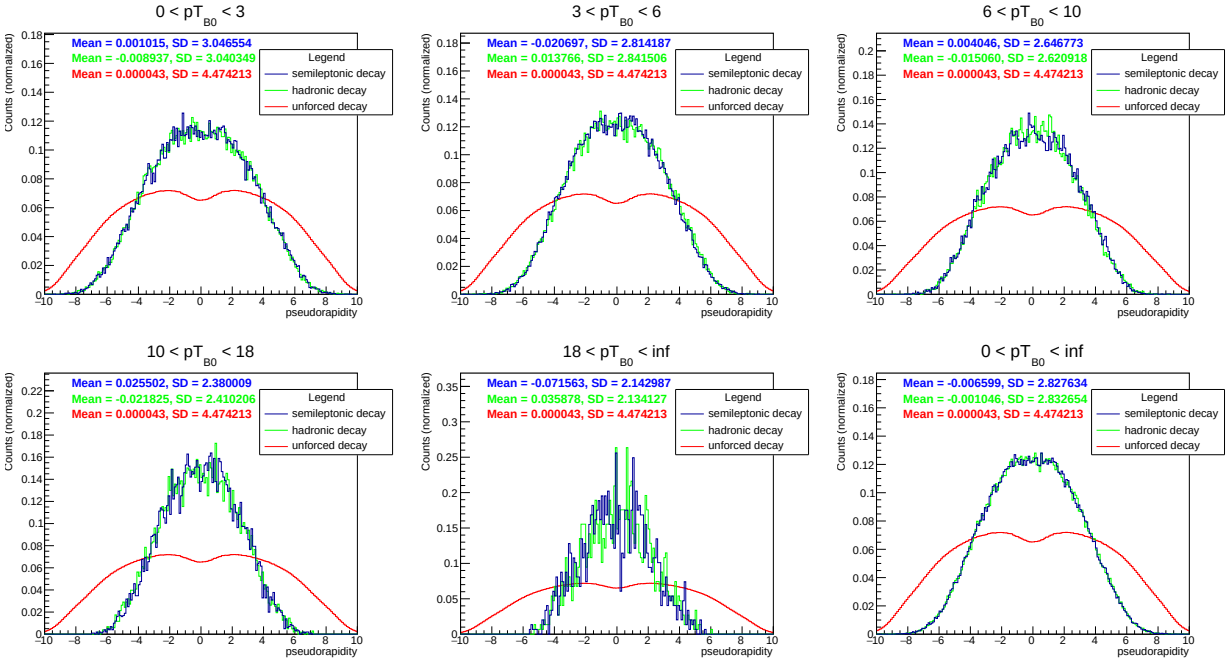

Figure 16: Comparison of η distributions for π^- in semileptonic, hadronic and unforced decays.

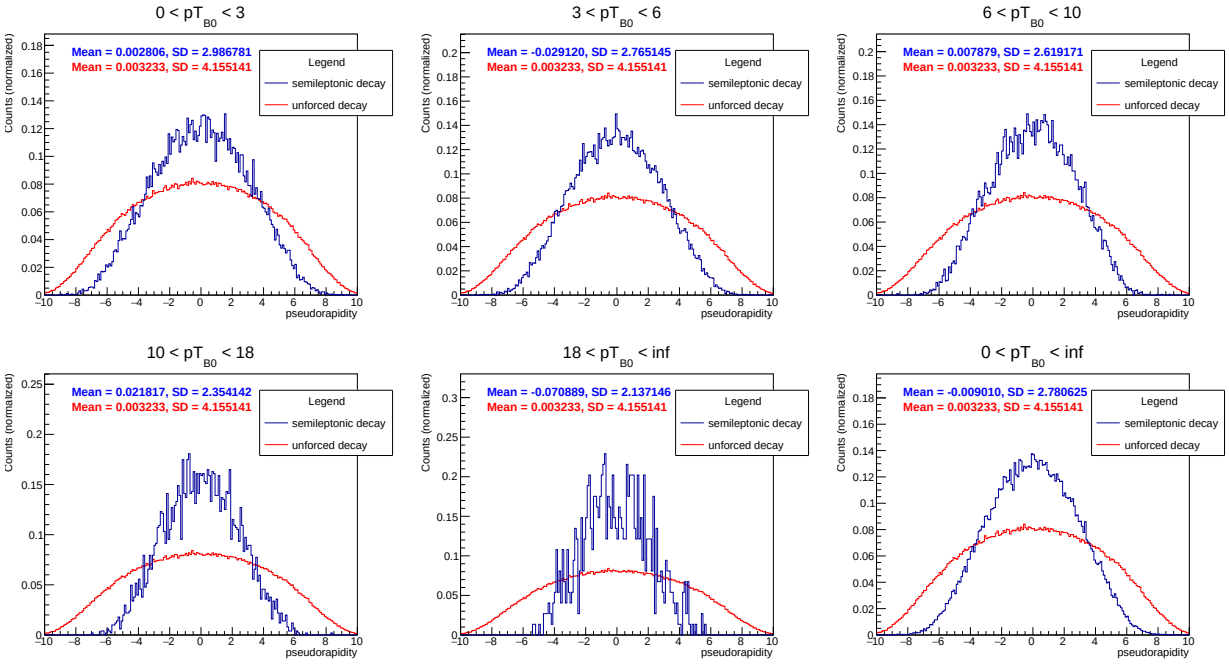

Figure 17: Comparison of η distributions for e^+ in semileptonic and unforced decays.

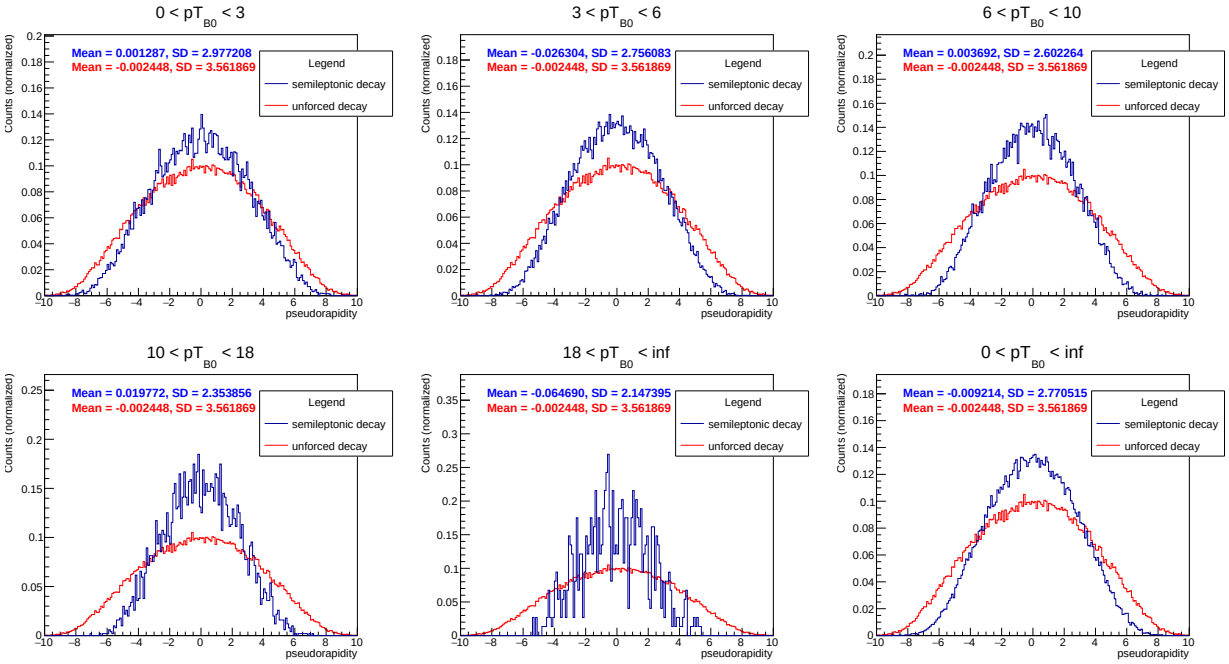

Figure 18: Comparison of η distributions for ν_e in semileptonic and unforced decays.

5.3 η difference distributions

In this section we will discuss the distributions of the differences in pseudorapidity between a particle and it mother, generated in the PYTHIA simulation. In the following figures, all y-axes are logarithmic.

In Figure 19, we see that here too the hadronic and semileptonic decay distributions of the D^- are in great agreement. The maximum of the distribution of the hadronic decay however, is lower than the maximum of the distribution of the semileptonic decay. At 0 GeV/c $< p_T^{B^0} <$ 3 GeV/c, we see that the peak of the decay of the semileptonic decay is flat, and the distribution of the hadronic decay has two separate peaks. The two distributions are wider than the background distribution until a pseudorapidity difference of ±4. At greater difference, the background distribution widens greatly. In higher p_T bins, distributions belonging to the decay channels are narrower than the background throughout. This means a cut on the maximum difference can remove background while retaining signal. However, this will only be productive at $p_T^{B^0} > 6$, because at lower p_T ranges the distributions of the hadronic and semileptonic decays are wider than the background. Taken over the entire p_T range, the distributions of the background and the hadronic and semileptonic decays are very much the same until a η difference of ±3.

Looking at Figure 20, we see that, for the K^+, the hadronic decay had a higher maximum than the semileptonic decay, and that both are well above the background. The difference between the background distribution and the other two distributions gets greater with greater $p_T^{B^0}$. The distributions of the decays also narrow with greater $p_T^{B^0}$. Here too, a cut in the maximum difference will yield separation of background and signal, but for the K^+, the cut can be imposed in all $p_T^{B^0}$ ranges.

Looking at the distributions of the π^- in Figure 21, we see the same pattern as with the K^+. The hadronic decay had the highest peak, with the semileptonic following and the background with the lowest maximum. All three distributions however are wider than we saw in Figure 20. The two decay channel distributions going from a maximum η difference of ~ ±4 at 0 GeV/c $< p_T^{B^0} <$ 3 GeV/c to a maximum of ~ ±2 at 10 GeV/c $< p_T^{B^0} <$ inf GeV/c. In contrast, in Figure 20 the maximum η difference went from ~ ±2 at 0 GeV/c $< p_T^{B^0} <$ 3 GeV/c to ~ ±1 at 10 GeV/c $< p_T^{B^0} <$ inf GeV/c. Because the distributions follow the same pattern, the same cut can be made in the maximum difference of the pseudorapidity.

For the e^+ in Figure 22 we see that the semileptonic distribution is wider and has a lower maximum than the background at a p_T of the B^0 smaller than 3 GeV/c. As $p_T^{B^0}$ increases, the distribution gets smaller, suggesting the same type of cut as seen previously. At 0 GeV/c $< p_T^{B^0} <$ 3 GeV/c, the distribution of the semileptonic decay has two peaks instead of one, like the background. In this case a cut on the minimum of the pseudorapidity difference could be productive, because the peak of the background distribution will then be removed. Taken over the entire p_T range, the distribution for the semileptonic decay is wider than the background distribution.

The distributions seen in Figure 23 are similar to those seen in Figure 22. The distributions for the semileptonic decay has two peaks and is wider than the background at 0 GeV/c $< p_T^{B^0} <$ 3 GeV/c. However, this distribution gets narrower ore quickly than the one of the e^+ and has a maximum already higher than the background at 6 GeV/c $< p_T^{B^0} <$ 10 GeV/c instead of at 10 GeV/c $< p_T^{B^0} <$ 18 GeV/c. Taken over the entire p_T range, the semileptonic distribution and the background distribution are almost indistinguishable.

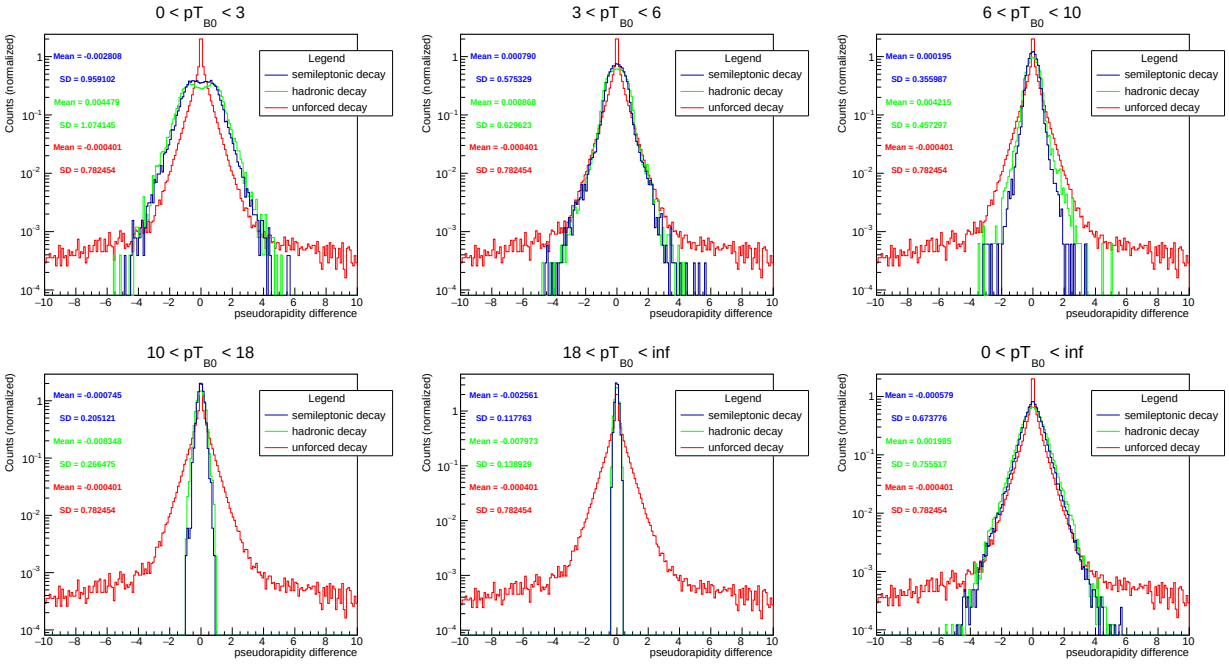

Figure 19: Comparison of difference in η distributions between D^- and their mother particle in semileptonic, hadronic and unforced decays

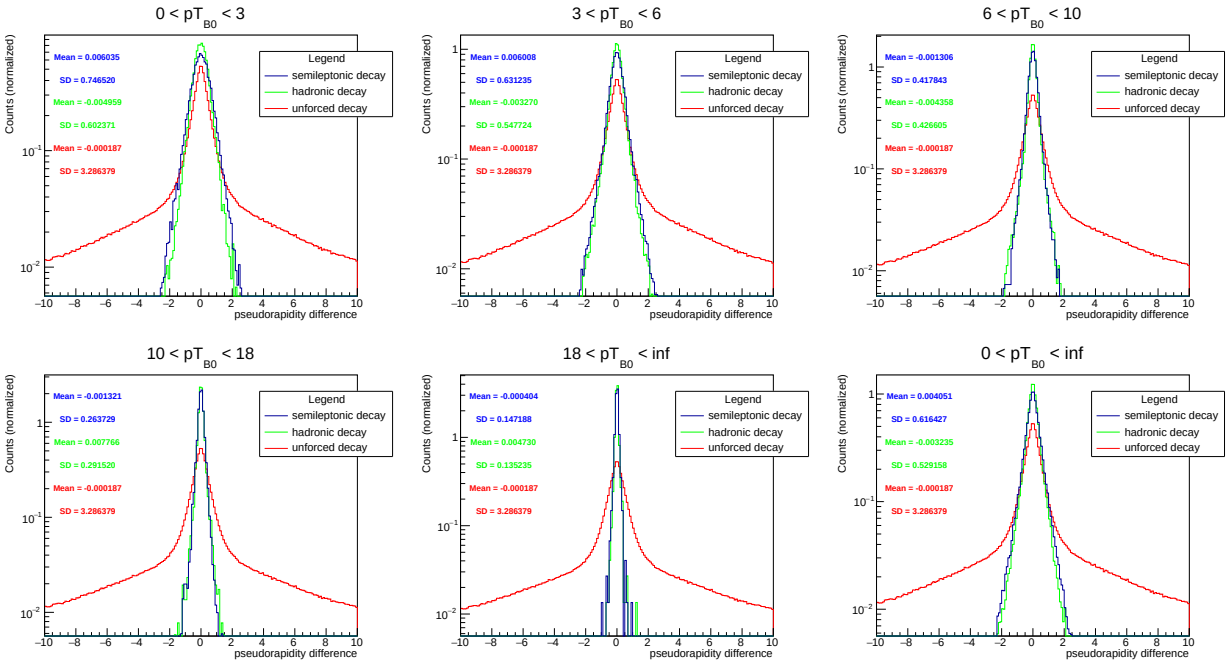

Figure 20: Comparison of difference in η distributions between K^+ and their mother particle in semileptonic, hadronic and unforced decays

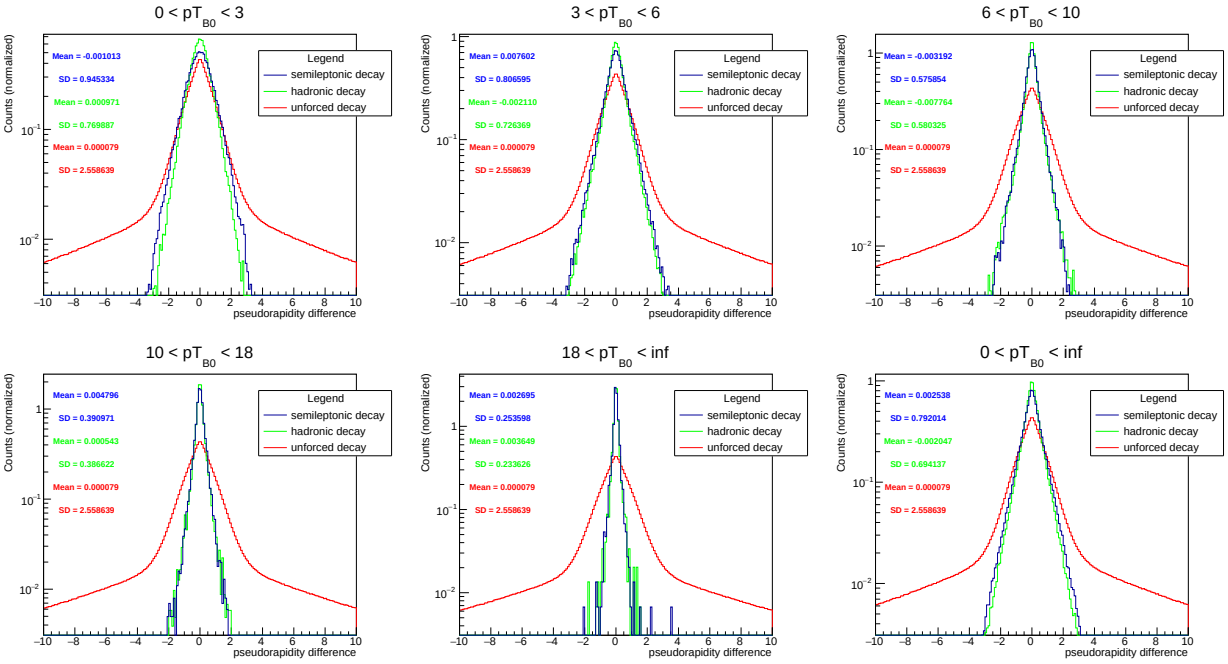

Figure 21: Comparison of difference in η distributions between π^- and their mother particle in semileptonic, hadronic and unforced decays

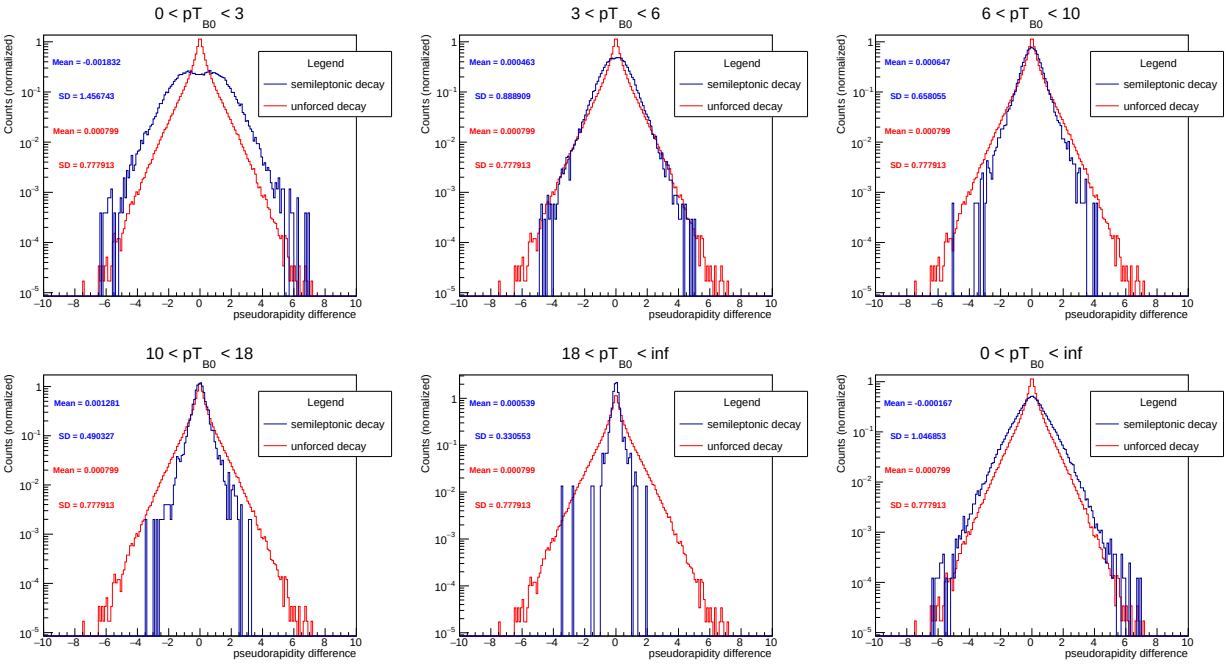

Figure 22: Comparison of difference in η distributions between e^+ and their mother particle in semileptonic and unforced decays

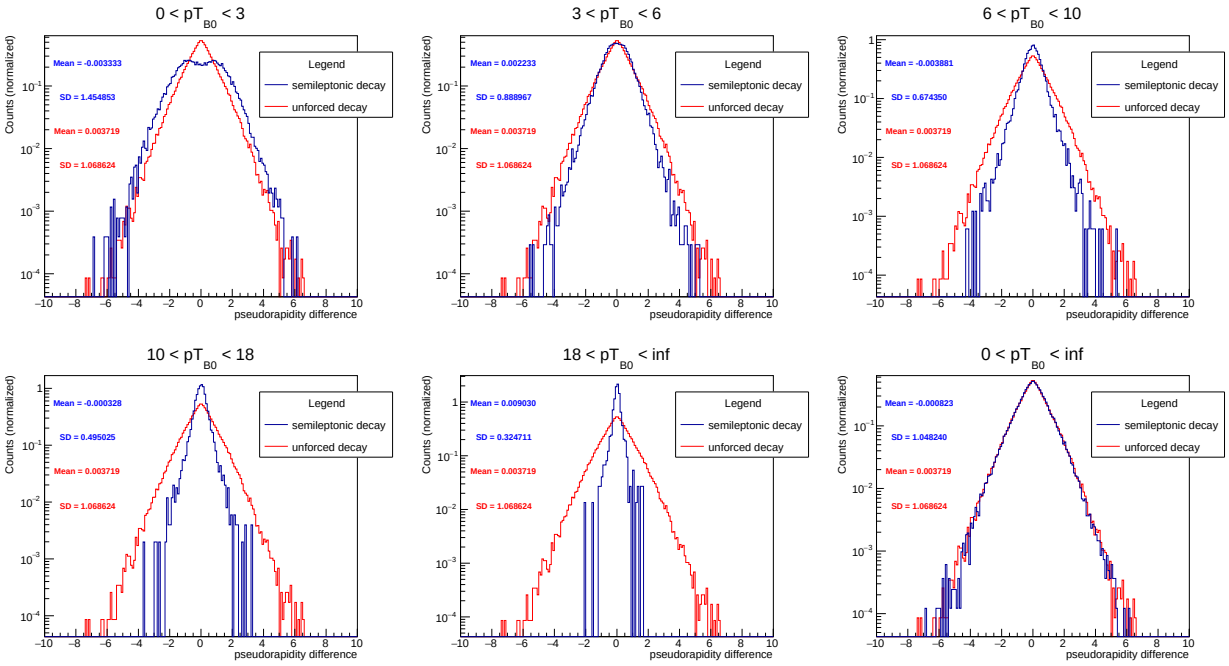

Figure 23: Comparison of difference in η distributions between ν_e and their mother particle in semileptonic and unforced decays

5.4 B^0 mass reconstruction

We will now consider the ALICE Monte Carlo simulations. As can be seen in Figure 24 and Table 2, in the 28 million events from the Monte Carlo simulation, it was possible to obtain around 9000 B0 candidates. After the cuts from Chapter 4.2, have been made this is reduced to 625 candidates. The cuts also have the effect of slightly shifting the distributions mean to a higher invariant mass, from 3.562 GeV/c^2 to 3.709 GeV/c^2, while decreasing its standard deviation. After the correction has been applied, the distribution has become much wider, mainly spread out in the higher invariant mass region. The standard deviation has increased substantially from 0.634 GeV/c^2 to 3.648 GeV/c^2. Comparing the candidates after the cut with the matched B^0 candidates we see that there are fewer matched B^0, namely 463, with a slightly higher mean and lower standard deviation. After the correction the distribution of matched candidates has a mean of 5.285 GeV/c^2, and a standard deviation of 2.167 GeV/c^2, both lower than the non-matched candidates.

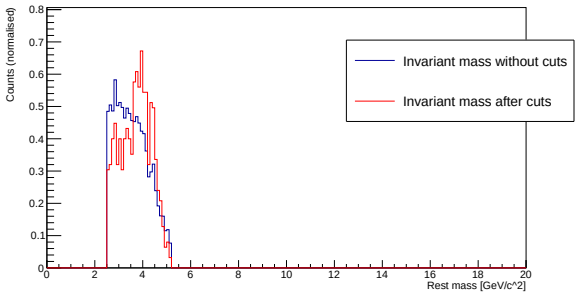

(a) D^-e^+ object invariant mass before and after cuts.

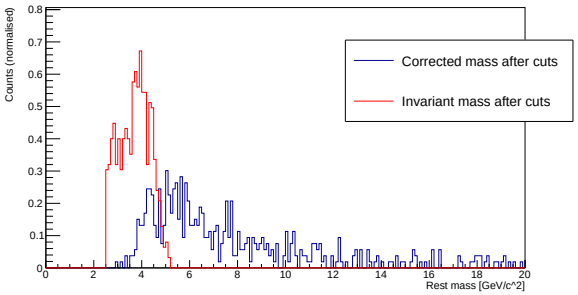

(b) D^-e^+ object invariant and corrected mass after cuts.

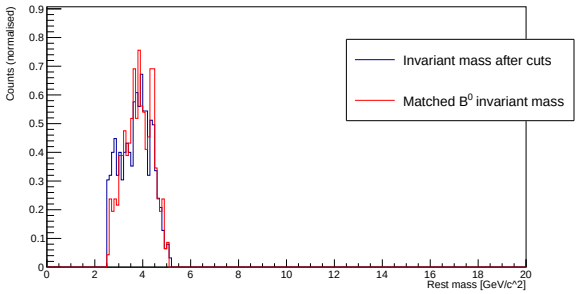

(c) D^-e^+ object after cuts and matched B^0 invariant mass.

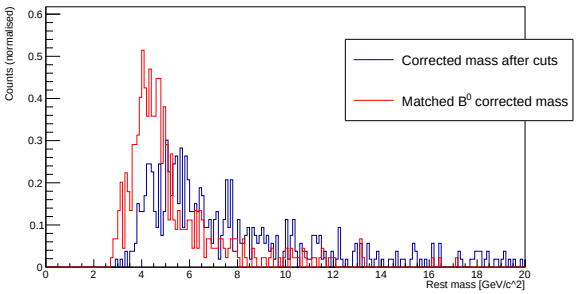

(d) D^-e^+ object after cuts and matched B^0 corrected mass.

Figure 24: Invariant mass distributions for 3 GeV/c < $p_T^{B^0}$ < inf GeV/c.

	Entries	Mean [GeV/c^2]	Standard deviation [GeV/c^2]
D^-e^+ object invariant mass before cuts	9114	3.562	0.6754
D^-e^+ object invariant mass after cuts	625	3.709	0.634
D^-e^+ object corrected mass after cuts	625	7.679	3.648
Matched B^0 invariant mass	463	3.819	0.5828
Matched B^0 corrected mass	463	5.285	2.167

Table 2: Amount of entries, mean and standard deviations of invariant mass distributions for 3 GeV/c < $p_T^{B^0}$ < inf GeV/c.

In Figure 25 and Tab;e 3 we can see the distributions for a B^0 p_T range between 3 GeV/c and 6 GeV/c. In this range there are 3755 candidates of which 179 remain after the cuts are applied. Here again, the mean is shifted slightly upward and the standard deviation is slightly lowered by the cuts. After The correction is applied, the distribution has a mean of 4.21 GeV/c^2instead of the earlier 3.514 GeV/c^2. Its standard deviation has increased from 0.6314 GeV/c^2 to 0.7843 GeV/c^2 and it has a few outliers above 6 GeV/c^2. There are an almost equal amount of matched and non matched B^0 candidates, although Figure 25c shows that there are differences in the make up of these sets. The distribution of matched candidates have a higher mean than the non-matched. After a correction to the matched B^0 candidates the mean increases to 4.12 GeV/c^2 and the standard deviation goes to 0.6693 GeV/c^2, both lower than those of the non-matched candidates.

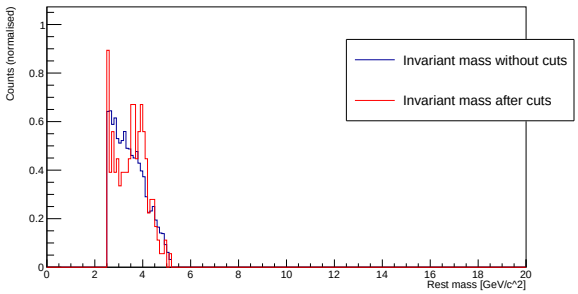

(a) D^-e^+ object invariant mass before and after cuts.

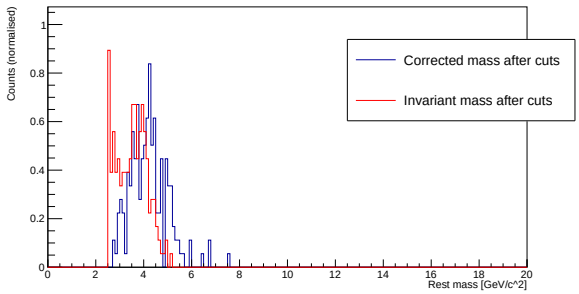

(b) D^-e^+ object invariant and corrected mass after cuts.

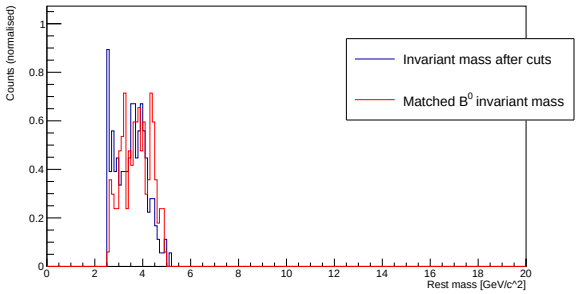

(c) D^-e^+ object after cuts and matched B^0 invariant mass.

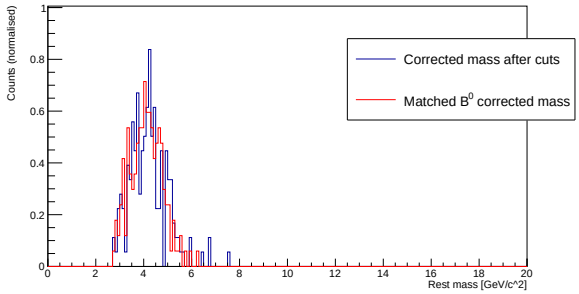

(d) D^-e^+ object after cuts and matched B^0 corrected mass.

Figure 25: Invariant mass distributions for 3 GeV/c $< p_T^{B^0} <$ 6 GeV/c.

	Entries	Mean [GeV/c^2]	Standard deviation [GeV/c^2]
D^-e^+ object invariant mass before cuts	3755	3.464	0.6527
D^-e^+ object invariant mass after cuts	179	3.514	0.6314
D^-e^+ object corrected mass after cuts	179	4.21	0.7843
Matched B^0 invariant mass	168	3.745	0.6023
Matched B^0 corrected mass	168	4.12	0.6693

Table 3: Amount of entries, mean and standard deviations of invariant mass distributions for 3 GeV/c $< p_T^{B^0} <$ 6 GeV/c.

In Figure 26 and Table 4 we see the distribution in the B^0 p_T range of 6 GeV/c and 10 GeV/c. Here we have 2599 candidates before the cuts and 199 afterwards. In contrast to the lower p_T ranges, the mean goes down instead of up after the cuts. However, the standard deviation still goes down. After the correction is made, the mean increases to 5.895 GeV/c^2 and the standard deviation to 2.05 GeV/c^2. The distribution has a tail leading into the higher mass ranges. The distributions of the matched candidates and the candidates after the cuts are similar. with their means and standard deviations being close to each other. After applying the correction, the mean of the distribution goes to 4.855 GeV/c^2 and its standard deviation to 1.445 GeV/c^2. These changes are smaller than those of the non-matched candidates.

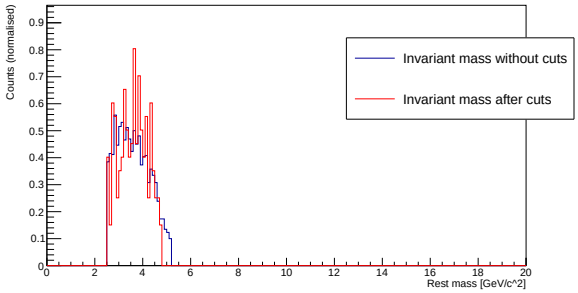

(a) D^-e^+ object invariant mass before and after cuts.

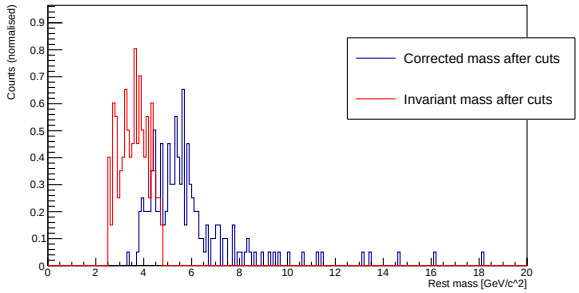

(b) D^-e^+ object invariant and corrected mass after cuts.

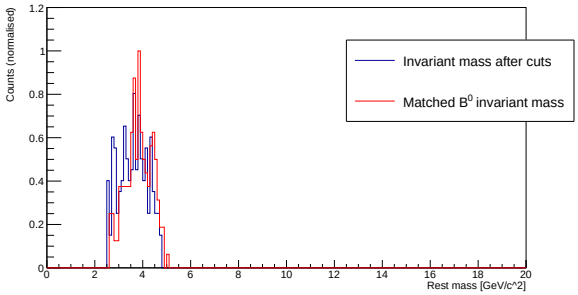

(c) D^-e^+ object after cuts and matched B^0 invariant mass.

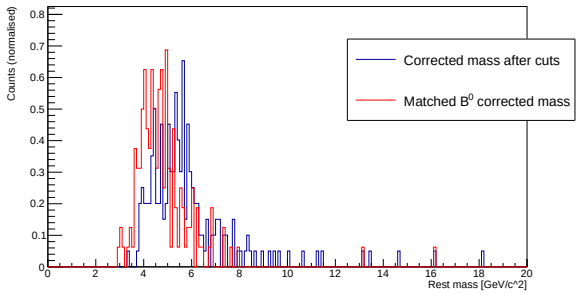

(d) D^-e^+ object after cuts and matched B^0 corrected mass.

Figure 26: Invariant mass distributions for 6 GeV/c < $p_T^{B^0}$ < 10 GeV/c.

	Entries	Mean [GeV/c^2]	Standard deviation [GeV/c^2]
D^-e^+ object invariant mass before cuts	2599	3.621	0.6784
D^-e^+ object invariant mass after cuts	199	3.608	0.5883
D^-e^+ object corrected mass after cuts	199	5.895	2.05
Matched B^0 invariant mass	160	3.831	0.5546
Matched B^0 corrected mass	160	4.855	1.445

Table 4: Amount of entries, mean and standard deviations of invariant mass distributions for 6 GeV/c < $p_T^{B^0}$ < 10 GeV/c.

Looking at Figure 27 and Table 5, we see that in the range 10 GeV/c < $p_T^{B^0}$ < inf GeV/c there are 2670 B^0 candidates before and 361 after the cuts, far more than the amount of matched candidates, which is 135. Here, the mean shifts upwards again after the cuts are made, while the standard deviation decreases. After the correction is made, the biggest changes yet happen. The mean goes from 3.789 GeV/c^2 to 9.781 GeV/c^2 and the standard deviation goes from 0.651 GeV/c^2 to 3.733 GeV/c^2. The matched candidates have a mean of 3.896 GeV/c^2 and a standard deviation of 0.5797 GeV/c^2. These also increase after the correction has been made, to respectively 7.51 GeV/c^2 ens 2.662 GeV/c^2.

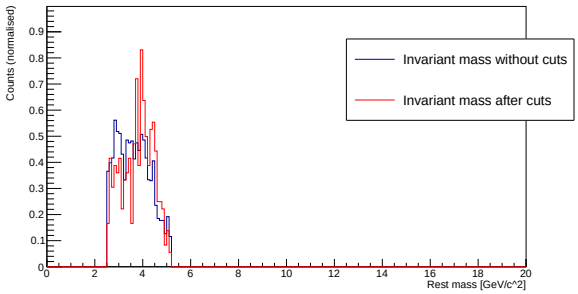

(a) D^-e^+ object invariant mass before and after cuts.

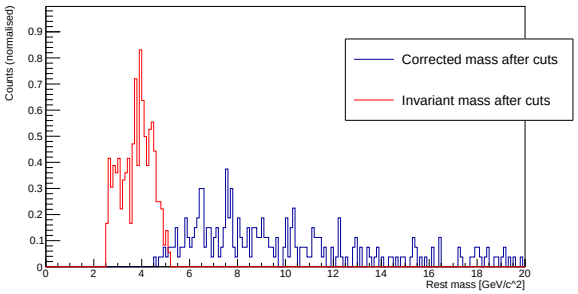

(b) D^-e^+ object invariant and corrected mass after cuts.

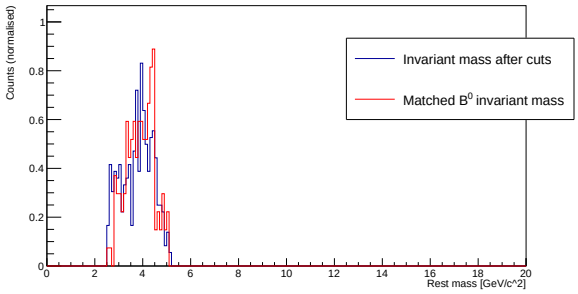

(c) D^-e^+ object after cuts and matched B^0 invariant mass.

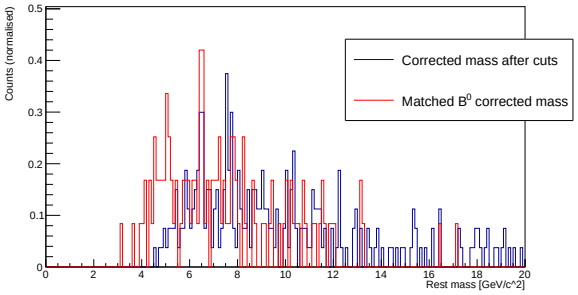

(d) D^-e^+ object after cuts and matched B^0 corrected mass.

Figure 27: Invariant mass distributions for 10 GeV/c < $p_T^{B^0}$ < inf GeV/c.

	Entries	Mean [GeV/c^2]	Standard deviation [GeV/c^2]
D^-e^+ object invariant mass before cuts	2760	3.642	0.6859
D^-e^+ object invariant mass after cuts	361	3.789	0.651
D^-e^+ object corrected mass after cuts	361	9.781	3.733
Matched B^0 invariant mass	135	3.896	0.5797
Matched B^0 corrected mass	135	7.51	2.662

Table 5: Amount of entries, mean and standard deviations of invariant mass distributions for 10 GeV/c < $p_T^{B^0}$ < inf GeV/c.

6 Conclusion

We have seen that there are differences in the characteristics of particles produces by our semileptonic decay of the B^0, a hadronic decay of the B^0 and background, which consists of particles which do not come from a B^0, but were reconstructed as such. The three p_T distributions were distinct from each other for all particles, albeit not for every $p_T^{B^0}$ range. Nevertheless, this means looking at the p_T distributions may be a good way to differentiate between background and B^0 daughters, especially at $p_T^{B^0} > 6\,\mathrm{GeV/c}$ where the distributions deviate from the background. One advantage the semileptonic decay offers over the hadronic decay is that the distribution of e^+, especially at $p_T^{B^0} < 3\,\mathrm{GeV/c}$, has its maximum and a large part of it distinct from the background distribution. This means that we can apply a cut on the minimum p_T of the e^+ to cut away a lot of background.

Looking at the pseudorapidity, we saw that the hadronic and semileptonic distributions were as good as inseparable. They were however very distinct from the background, which is useful in determining which particles are daughters of the B^0 and which are not. Especially at $p_T^{B^0} >\sim 6\,\mathrm{GeV/c}$ ranges where the distributions narrow. There, a cut on the maximum η can be imposed to cut away a great deal of background. The mesonic daughters also offer the extra advantage of the background having a two peak structure while at $p_T^{B^0} >\sim 3\,\mathrm{GeV/c}$ the daughters do not, creating a more distinct signal. Here, a tighter cut in the maximum η can be imposed. However, this is true for the semileptonic as well as the hadronic decay, offering the semileptonic no distinct advantage in this regard. Furthermore, the ALICE detector can only reconstruct particles for $|\eta| < 0.9$. This means that these findings cannot be used in their entirety.

For the differences in pseudorapidity, the distributions of the two decay channels were less similar than they were concerning the pseudorapidity itself, but their differences were still small. At $p_T^{B^0} > 6\,\mathrm{GeV/c}$ they were distinct from the background, notably by being narrower, suggesting a cut in the maximum η difference. The semileptonic decay channel offers an extra option here over the hadronic decay, by having the e^+ distribution to look at. This distribution has a two peaked structure at $p_T^{B^0} 3\,\mathrm{GeV/c}$, which the background does not, providing the opportunity to find a better signal using a cut on the minimum of the difference in pseudorapidity.

Concerning the reconstruction of the invariant mass of the B^0 we mainly saw that the method of reconstructing the missing p_T had diverse effects depending on the p_T bin of the B^0. The higher the $p_T^{B^0}$, more influence the correction had. This is due to the fact that $p_{T_{missing}}$ is a function of $p_T^{B^0}$. It is interesting to note that, while in no p_T bin the correction helped set the invariant mass to the theoretical value, integrated over all bins, the matched candidates provided a corrected invariant mass very close to it ($5.285\ \mathrm{GeV/c^2}$), albeit with a standard deviation of $2.167\ \mathrm{GeV/c^2}$. Also relevant is the fact that in the p_T range from 10 GeV/c and up, there were many more B^0 candidates after the cuts than matched B^0 candidates. Because in the other p_T bins the B^0 candidates after cuts were closer in number to the matched candidates, this means that the candidates from the the high p_T bin were over-represented in the overall invariant mass reconstruction. Combined with the fact that the correction has a stronger effect on candidates from a higher p_T bin, this can help explain why the corrected B^0 invariant mass became $7.679\ \mathrm{GeV/c^2}$, which is too high. A possible remedy to this problem is to impose more stringent cuts in the p_T bin.

This leads us to possible further research. There could be more research as to which cuts in which variables provide the best results. Furthermore, one could examine whether the extra possibilities and advantages of using this semileptonic decay channel in data analysis outweighs the lower branching ratio it has compared to the hadronic decay, as the aim of this thesis was only to explore the *what* advantages the semileptonic decay offers.

All in all, analysis using the semileptonic has certain advantages, such as more ways to cut in variables as to better distinguish signal from background, and certain disadvantages, such as the uncertainty in the invariant mass which can only be reconstructed by approximation and its lower branching ratio. Whether the advantages outweigh the disadvantages remain to be seen.

References

[1] Gouranga C Nayak. "Hadron Formation From Quark-Gluon Plasma Using Lattice QCD At Finite Temperature". In: *arXiv preprint arXiv:1902.10522* (2018).

[2] Y. Nagashima and Y. Nambu. *Elementary Particle Physics: Quantum Field Theory and Particles*. v. 1. Wiley, 2010. ISBN: 9783527630103. URL: https://books.google.nl/books?id=J0l8s3pdOksC.

[3] MissMJ. *Standard Model of Elementary Particles*. [Online; accessed May 14, 2019]. 2019. URL: https://commons.wikimedia.org/w/index.php?curid=4286964.

[4] CMS. [Online; accessed May 14, 2019]. 2012. URL: https://cms-docdb.cern.ch/cgi-bin/PublicDocDB/RetrieveFile?docid=5703&version=1&filename=Susy_1.4.jpg.

[5] John Christian Lequiron and Harry Casimir Merida. [Online; accessed May 14, 2019]. 2012. URL: http://rtuparticlephysics.blogspot.com/2012/10/the-fundamental-particles-and-product.html.

[6] Lennart van Doremalen. "Beauty of the Quark Gluon Plasma". MA thesis. Utrecht University, Feb. 2017.

[7] J. Greensite. *An Introduction to the Confinement Problem*. Lecture Notes in Physics. Springer Berlin Heidelberg, 2011. ISBN: 9783642143816. URL: https://books.google.nl/books?id=CP7%5C_QooHo8wC.

[8] Helmut Satz. "The Quark-Gluon Plasma". In: *arXiv preprint arXiv:1101.3937* (2011).

[9] M. Tanabashi et al. "Review of Particle Physics". In: *Phys. Rev. D* 98 (3 Aug. 2018), p. 030001. DOI: 10.1103/PhysRevD.98.030001. URL: https://link.aps.org/doi/10.1103/PhysRevD.98.030001.

[10] Ralf Rapp and Hendrik van Hees. "Heavy Quarks in the Quark-Gluon Plasma". In: (2010), pp. 111–206. DOI: 10.1142/9789814293297_0003. arXiv: 0903.1096 [hep-ph].

[11] *ALICE homepage*. http://alice.web.cern.ch/. Accessed: 2019-05-28.

[12] Betty Bezverkhny Abelev et al. "Performance of the ALICE Experiment at the CERN LHC". In: *Int. J. Mod. Phys.* A29 (2014), p. 1430044. DOI: 10.1142/S0217751X14300440. arXiv: 1402.4476 [nucl-ex].

[13] S. Beolè. "The ALICE Inner Tracking System: Performance with Proton and Lead Beams". In: *Physics Procedia* 37 (2012). Proceedings of the 2nd International Conference on Technology and Instrumentation in Particle Physics (TIPP 2011), pp. 1062–1069. ISSN: 1875-3892. DOI: https://doi.org/10.1016/j.phpro.2012.02.443. URL: http://www.sciencedirect.com/science/article/pii/S1875389212017981.

[14] Christian Lippmann et al. "The Time Projection Chamber for the ALICE Experiment". In: *arXiv preprint arXiv:0809.5133* (2008).

[15] Francesca Carnesecchi. "Performance of the ALICE Time-Of-Flight detector at the LHC". In: *arXiv e-prints*, arXiv:1806.03825 (June 2018), arXiv:1806.03825. arXiv: 1806.03825 [physics.ins-det].

[16] JabberWok. *Pseudorapidity2*. [Online; accessed May 29, 2019]. 2007. URL: https://commons.wikimedia.org/wiki/File:Pseudorapidity2.png.

[17] Torbjörn Sjöstrand, Stephen Mrenna, and Peter Skands. "A brief introduction to PYTHIA 8.1". In: *Computer Physics Communications* 178.11 (2008), pp. 852–867.

[18] R. Brun and F. Rademakers. "ROOT: An object oriented data analysis framework". In: *Nucl. Instrum. Meth.* A389 (1997), pp. 81–86. DOI: 10.1016/S0168-9002(97)00048-X.

[19] C. Bedda. *B0->D- e+ nu e analysis*. Presentation. 2016.